Available online at www.sciencedirect.com
ScienceDirect
Journal of Solid State Chemistry 181 (2008) 1298–1306
JOURNAL OF SOLID STATE CHEMISTRY
www.elsevier.com/locate/jssc

CTAB assisted hydrothermal synthesis, controlled conversion and CO oxidation properties of CeO_2 nanoplates, nanotubes, and nanorods

Chengsi Pan[a,b], Dengsong Zhang[a,b,*], Liyi Shi[a,b]

[a]*Research Center of Nano Science and Technology, Shanghai University, Shanghai 200444, China*
[b]*Department of Chemistry, Shanghai University, Shanghai 200444, China*

Received 13 November 2007; received in revised form 3 February 2008; accepted 4 February 2008
Available online 25 February 2008

Abstract

In this work, CeO_2 nanoplates were synthesized by a hydrothermal reaction assisted by hexadecyltrimethylammonium bromide (CTAB) at 100–160 °C. The size of nanoplates was around 40 nm. Further experiment showed that the controlled conversion of nanoplates into nanotubes, and nanorods can be realized by changing the reaction time, temperature, and CTAB/Ce^{3+} ratio value. X-ray diffraction (XRD), transmission electron microscopy (TEM), and Brunauer–Emmett–Teller (BET) nitrogen adsorption–desorption measurements were employed to characterize the samples. The CO oxidation properties of nanorods, nanoplates, and nanotubes were investigated. An enhanced catalytic activity has been found for CO oxidation by using CeO_2 nanoplates as compared with CeO_2 nanotubes and nanorods, and the crystal surfaces (100) of CeO_2 nanoplates were considered to play an important role in determining their catalytic oxidation properties.

Keywords: Ceria; Nanoplate; Nanotube; Nanorod; CO oxidation

1. Introduction

Ceria (CeO_2) has been extensively applied in heterogeneous catalysis [1], solid oxide fuel cells (SOFCs) [2], optics [3], polishing materials [4], gas sensors [5], UV blockers [6], especially in three-way catalysts (TWCs) [7,8]. In recent years, CeO_2 nanostructured materials have received a tremendous amount of attention because of their unique properties derived from a low dimensionality and a high surface area.

Over the past few years, CeO_2 nanostructured materials with various morphologies, such as, nanoparticles [9], nanorods [10], nanotubes [11], and core-shell nanowires [12] have been prepared by us and other research groups. Recently, nanoplates have attracted increasing attention due to two advantages: one is high crystallinity and well-defined chemical composition as well as extremely high anisotropy with an ultrathin thickness [13] and the other is that they are superior precursors to be used for conversion into other nanostructrures [14], such as nanotubes based on the rolling-up mechanism. Thus, CeO_2 nanoplates are hoped to be synthesized so that they can improve the catalytic performance and also be easy to convert into other useful nanostructures. Recently, Yang et al. [15] synthesized the cubic CeO_2 plate with size of 8 nm in the toluene and water mixture using oleic acid as capping regnant under hydrothermal conditions. However, no reports on synthesis and conversion of CeO_2 nanoplates ($D > 10$ nm) have been published up to date.

CeO_2 is potential to be widely used in catalysis due to the activity of the surface vacancy determined by the CeO_2 crystal surface. Mai et al. [16] synthesized ceria with various shapes using a hydrothermal method, and experimentally observed that ceria nanorods showed the highest oxygen-storage capacity. They thought that the (110) and (100) surfaces of the CeO_2 nanorods resulted in the superior performance. Zhou et al. [17] converted CeO_2 nanorods into nanotubes in an H_2O_2 solution assisted by ultrasonication, and the nanotubes showed highly

*Corresponding author at: Research Center of Nano Science and Technology, Shanghai University, Shanghai 200444, China.
Fax: +86 21 66134852.
E-mail address: dszhang@shu.edu.cn (D. Zhang).

0022-4596/$ - see front matter © 2008 Elsevier Inc. All rights reserved.
doi:10.1016/j.jssc.2008.02.011

reducible property, which was due to the higher activity of CeO_2 surface (100) than that of common surface (111). Several reports on the relationship between the crystal surface and the catalytic activity of one-dimensional CeO_2 demonstrated by both experiments and computing have been published. However, the catalytic activity of two-dimensional CeO_2 nanoplates has never been investigated.

Recently, we have already synthesized CeO_2 nanorods assisted by PEG600 as a capping regnant with an ultrasonic method [10] and CeO_2 nanotubes assisted by carbon nanotubes with a liquid phase deposition method [18,19]. Herein we firstly report a simple method to synthesize the CeO_2 nanoplates assisted by hexadecyltrimethylammonium bromide (CTAB) under a hydrothermal condition, and controlled conversions of nanoplates into nanotubes and nanorods are realized by changing the reaction time, temperature, and CTAB/Ce^{3+} ratio value. An enhanced catalytic activity for CO oxidation is found for CeO_2 nanoplates compared with CeO_2 nanotubes and nanorods.

2. Experimental section

2.1. Preparation

Analytical grade $Ce(NO_3)_3 \cdot 6H_2O$, CTAB, and $NH_3 \cdot H_2O$ were purchased from National Chemical Company (Shanghai, China) and were used without further purification. Deionized water was used throughout. The reaction was carried out in a 50 mL capacity Teflon-lined stainless steel autoclave, and in a digital-type temperature-controlled oven.

In a typical procedure, 3 mmol $Ce(NO_3)_3 \cdot 6H_2O$ and 1 mmol CTAB were mixed together in a beaker under stirring. The 4 mL $NH_3 \cdot H_2O$ was added to the mixed solution, and then the mixture was transferred into a 50 mL capacity Teflon-lined stainless steel autoclave. Subsequently, the autoclave was laid in an oven at 100 °C for 24 h. The products were washed with deionized water for three times and dried at 80 °C for 24 h. The as-prepared product was denoted as S1. Other samples (S2–S10) were prepared by the similar procedure with various conditions as shown in Table 1.

2.2. Catalytic activity evaluation

The catalytic activities for CO oxidation were evaluated in a U-shaped quartz reactor. The catalyst particles (0.15 g) were placed in the reactor. The reactant gases (1.0% CO, 28% O_2, balanced with nitrogen) went through the reactor at a rate of 40 mL/min. The composition of the gas exiting the reactor was monitored by gas chromatography.

2.3. Material characterization

The as-prepared samples were characterized by X-ray diffraction (XRD, Rigaku D/max2500PC) with Cu $K\alpha$ radiation. The samples were observed by a field emission high resolution transmission electron microscope (HRTEM, JEOL JEM-2010F) and powdered samples were dispersed in absolute ethanol by ultrasonication for 10 min in a KQ-250B ultrasonic bath. Brunauer–Emmett–Teller (BET) specific surface area of the samples was characterized by nitrogen adsorption at 77 K with Micromeritics ASAP 2010. Images were analyzed using Image-Pro-Plus 5.0. At least 500 nanoparticles were counted and sized for each sample.

3. Results and discussion

3.1. Characteristics and influence factors of CeO_2 nanoplates, nanotubes, and nanorods

The phase purity and crystal structure of the CeO_2 nanorods, nanoplates, and nanotubes obtained are first examined by XRD pattern (Fig. 1). The sample exhibits

Table 1
Summary of the experimental conditions and the corresponding morphologies and dimensions of the samples

Sample	Molar ratio CTAB:Ce^{3+}	Reaction time (h)	Temperature (°C)	Morphology	Length (nm) * Diameter (nm)
S1	1:3	24	100	Cubic plate	17
S2	1:3	24	120	Irregular plate	40
S3	1:3	24	140	Nanoplates with hexagon and cubic shape	20
S4	1:3	24	160	Nanoplates with hexagon shape	15
S5	1:3	48	100	Nanoplates with hexagon shape	50
S6	1:3	72	100	Nanorods and nanoplates with hexagon shape	20 * 100 (nanorods) 40 (nanoplates)
S7	2:3	2	100	nanoplates	20
S8	2:3	8	100	nanotubes	25 * 200
S9	2:3	24	100	nanorods	20 * 500
S10	2:3	72	100	Nanorods and nanoparticles	15 * 150 (nanorods) 10 (nanoparticles)

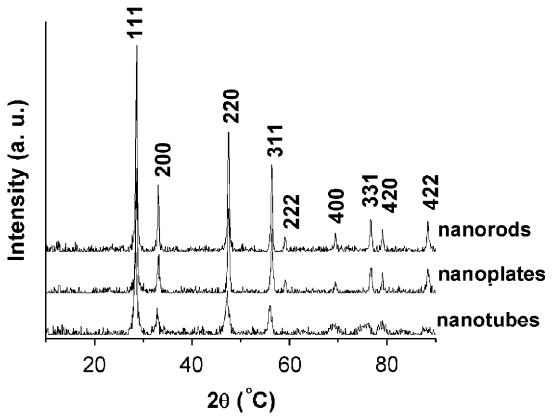

Fig. 1. XRD patterns of the as-prepared CeO_2 nanostructures.

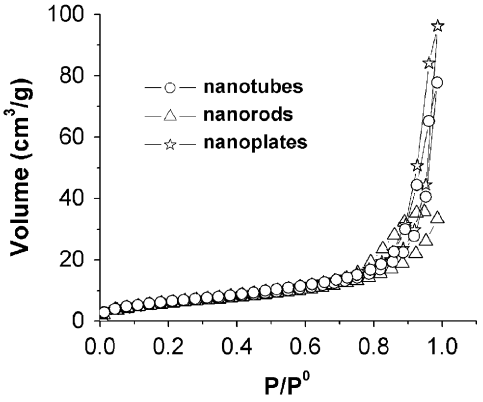

Fig. 2. Nitrogen adsorption–desorption isotherms for CeO_2 nanostructures: nanoplates (S2), nanotubes (S9), and nanorods (S8).

XRD peaks that correspond to the (111), (200), (220), (311), (222), (400), (331), (420), and (422) planes of a cubic fluorite structure (space group: $Fm3m$) of CeO_2 as identified using the standard data JCPDS 34-0394. The average crystallite sizes (D) of CeO_2 nanorods, nanoplates, and nanotubes calculated from X-ray line broadening of the reflections of (111) using Scherrer's equation are 22.4, 25.1, and 17.2 nm, respectively. The values of the lattice parameter for the nanorods, nanoplates, and nanotubes calculated from the XRD spectra are 0.5402, 0.5357, and 0.5405 nm, respectively. It is noted that the values of the lattice parameter for CeO_2 nanostructures are lower than that reported for the bulk CeO_2 which is 0.5413 nm in the standard data JCPDS 34-0394. It may be explained that the CTA^+ groups may stabilize the small nanoparticles and reduce the surface relaxation of the forming nanoparticles resulting in smaller values of the lattice parameters in our samples, as proposed by Maensiri et al. [20].

Fig. 2 shows the nitrogen adsorption–desorption isotherms of CeO_2 nanorods, nanoplate, and nanotubes. The materials exhibit a large BET specific surface area: 80.1 m^2/g for nanotubes, 52.5 m^2/g for nanorods, and 37.2 m^2/g for nanoplates, respectively. The hysteresis loops are all at P/Po 0.8–1.0, which indicates a microporous material. Nanoplates exhibit a type B hysteresis loop which is typical of slit-shaped pores or the space between parallel plates based on the BDDT classification, while nanotubes and nanorods exhibit a type C hysteresis loop due to a mixture of tapered or wedge-shaped pores with open ends [21,22].

The morphologies of the products are summarized in Table 1. It is found that the reaction time, the CTAB/Ce^{3+} value, and the temperature of the solutions have great effects on the morphologies of the final products, which is shown in the following paragraphs.

Fig. 3 shows the morphologies of the samples prepared at various hydrothermal temperatures. The morphology of the corresponding products is an obvious plate but the size on average is different. The nanoplate is mostly cubic at 100 °C (Fig. 3a), while it is irregular at 120 °C (Fig. 3b). The cross-section TEM image shows that the thickness of nanoplates is ~3 nm (Fig. 3b, inset). The percentage of irregular plates decreases, while that of rhombic and hexagonal plates increases at 140 °C (Fig. 3c). At 160 °C, few irregular plates but rhombic and hexagonal plates as the sole product are observed in Fig. 3d. For a face-centered cubic (fcc) ceria crystal, as illustrated by Zhou et al. [23], the shape of the nanocrystals is mainly tetradecahedron (Fig. 3f, inset) whose surface is composed of planes (100) and (111). The shape of the crystals self-assembled by (111) is rhombic or hexagonal (Fig. 3e), while that by (100) is cubic (Fig. 3f), due to that CTAB absorbs on the exposed surface of CeO_2 crystal and limits to grow.

The particle size distribution is shown in Fig. 4. At 100 °C, the size of plates is around 17 nm (>60%), and it has a narrow distribution. It is interesting that with the temperature rising, the size of plates increases initially and then decreases. The size is around 40 nm (>60%) at 120 °C, while that is around 20 nm (>70%) at 140 °C and around 15 nm at 160 °C. On the basis of TEM images and the shape analysis, the plate is cubic with the exposed surface (100) at low hydrothermal temperature, also reported by Gao and his coworkers [15], while the plate is rhombic or hexagonal with the exposed surface (111) at high hydrothermal temperature.

The pore size distribution based on BJH model of samples prepared at various temperatures is shown in Fig. 5. The samples prepared at 100–140 °C show a similar peak between 30 and 40 nm (Fig. 5a–c), where the wide pore-size distribution is due to the open space between the parallel planes according to the adsorption–desorption isotherms. Similar isotherms are also obtained for S1 and S3 (see supporting information Fig. S1). The sample prepared at 160 °C shows a peak at 20 nm (Fig. 5d), where the small pore diameter and pore volume show a compact structure of the rhombic or hexagonal CeO_2.

The influences of hydrothermal time and CTAB/Ce^{3+} ratio value on the morphology of the product are also investigated. When CTAB/Ce^{3+} ratio value is 1:3, the

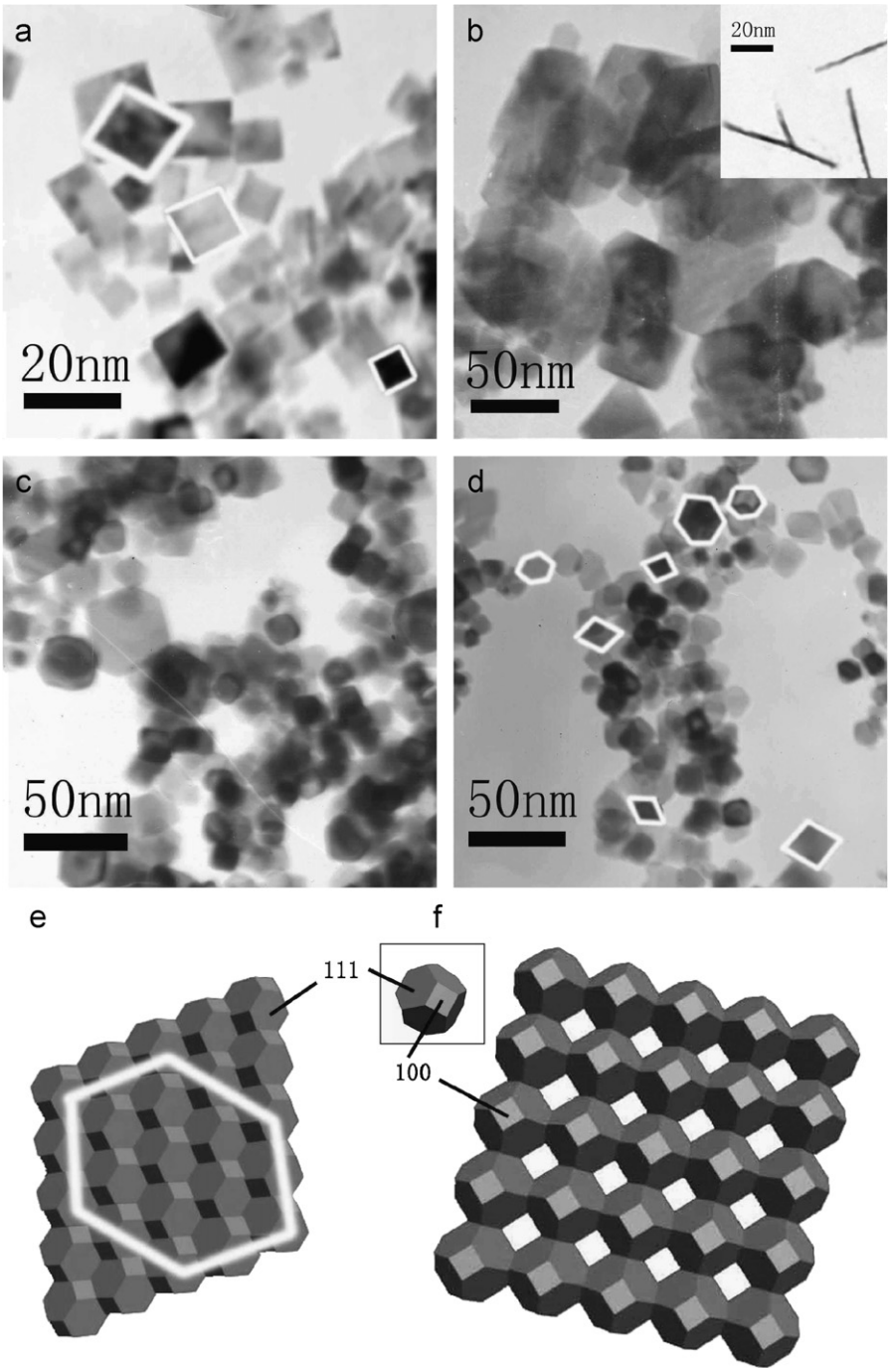

Fig. 3. TEM images of the CeO_2 nanoplates under CTAB/Ce^{3+} = 1:3 for 24 h at various temperatures: (a) 100 °C (white line indicates the cubic structure), (b) 120 °C (inset is the cross-section TEM image of nanoplates), (c) 140 °C, (d) 160 °C (white line indicates the rhombic or hexagonal structure); and the CeO_2 crystal models (inset is the tiny nanocrystal): (e) rhombic (white line indicates the hexagonal structure), and (f) cubic.

thickness of nanoplates increases with the hydrothermal time increasing (Fig. 6a) and a few nanorods appear when the hydrothermal time is up to 72 h (Fig. 6b), which implies nanoplates can be converted to nanorods by the change of the hydrothermal time. When CTAB/Ce^{3+} ratio value is changed to 2:3, CeO_2 nanoplates firstly form at ~2 h under hydrothermal conditions, which is shown in Fig. 6c. With the reaction time increasing to 6 h, nanoplates are partly converted to nanotubes as observed in Fig. S2, while with the reaction time increasing to 8 h, the sole products as nanotubes are observed in Fig. 6d, indicating that nanotubes are evolved from nanoplates. The open tip of nanotubes can be clearly observed in Fig. 6d. Fig. 6c (inset) and d (inset) shows that both nanorods and nanotubes display a cross-lattice pattern with a lattice spacing of 0.19 nm, corresponding to the interplanar separation between the {220} or {022} lattice planes of cubic ceria, which implies the exposure surface is (110). It is interesting

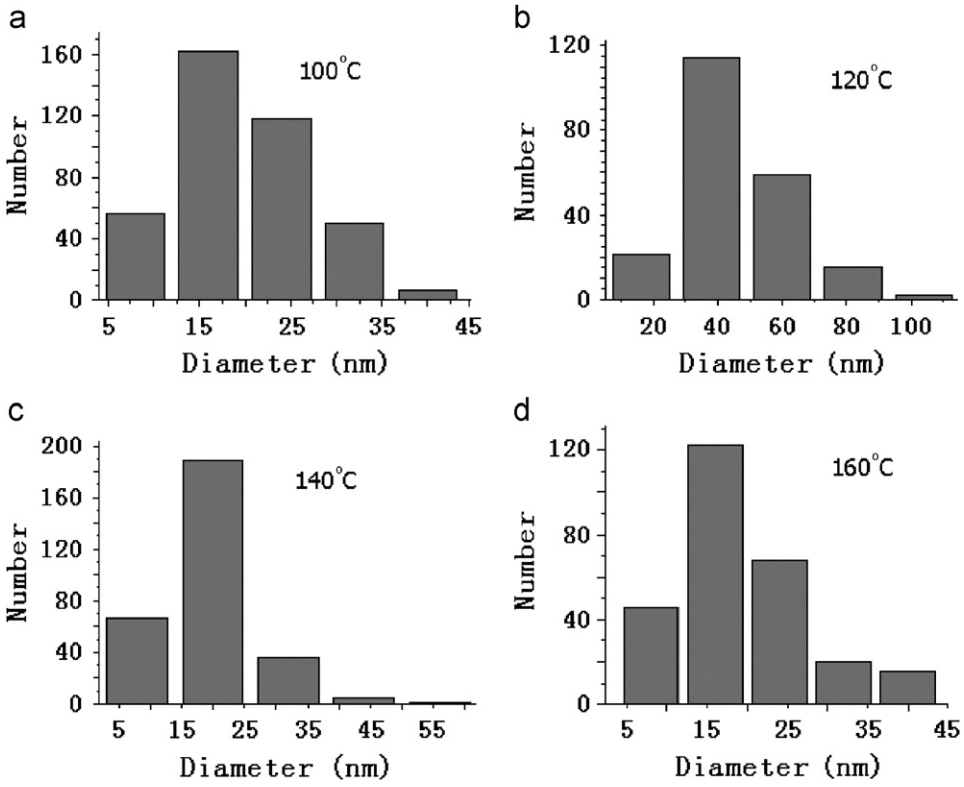

Fig. 4. Particle size distribution of the CeO_2 nanoplates under CTAB/Ce^{3+} = 1:3 for 24 h at various temperatures: (a) 100 °C, (b) 120 °C, (c) 140 °C, and (d) 160 °C.

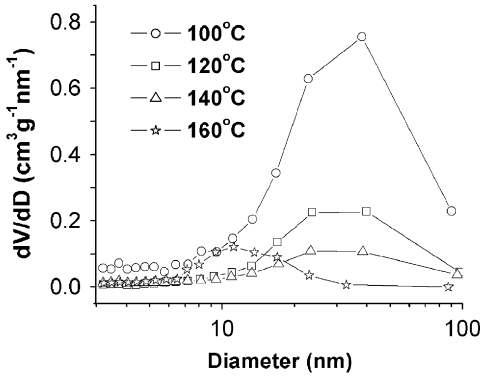

Fig. 5. Plot of the pore volume vs. pore diameter for various CeO_2 nanoplates.

that nanotubes are converted to nanorods with the hydrothermal time further increasing (Fig. 6e) and finally the nanorods collapse when the hydrothermal time is long enough (Fig. 6f).

The pore structure of the samples is evaluated by N_2 adsorption, as shown in Fig. 7. It is obvious that nanotubes mainly have two kinds of pores: one is at 4 nm and the other is at 20 nm. The former is attributed to inner structures of nanotubes, while the latter is attributed to stacks of nanotubes. The nanorods have the smallest pores, which indicate the compact structures of the nanostructures. The pores of nanoplates are a bit larger than those of nanotubes and nanorods (Fig. 7), which may be due to the two-dimensional structure of nanoplates.

3.2. *Possible formation and conversion mechanisms of CeO_2 nanoplates, nanotubes, and nanorods*

The above-mentioned experiments demonstrate that the shape evolutions of CeO_2 nanocrystals could be controlled and influenced by some factors such as reaction time, reaction temperature, and CTAB/Ce^{3+} ratio value in the initial solution. Scheme 1 shows the possible formation mechanism of CeO_2 with different morphologies.

The previous experiment shows CeO_2 nanoparticles exhibit negative charges when the pH value is higher than 7.8 [24]. In our experiment, CTA^+ is firstly absorbed on the surface of CeO_2 nanoparticles. The absorbed ligand molecules are likely to interact preferentially with the (111) surface plane to (100) at low temperature which is demonstrated by Vantomme et al. [25]. The exposed surfaces tend to combine together to reduce the surface energy to form a cubic plane structure (Fig. 3a, b, and f). As temperature increases, CeO_2 nanoplates show a rhombic or hexagonal shape in the TEM images (Fig. 3c–e) due to the absorption force between the CTA^+ and the surface of CeO_2 nanoparticles decreasing. Thus, they prefer to combine with (111) surface due to their fcc structure, as Wang et al. reported, where the surface

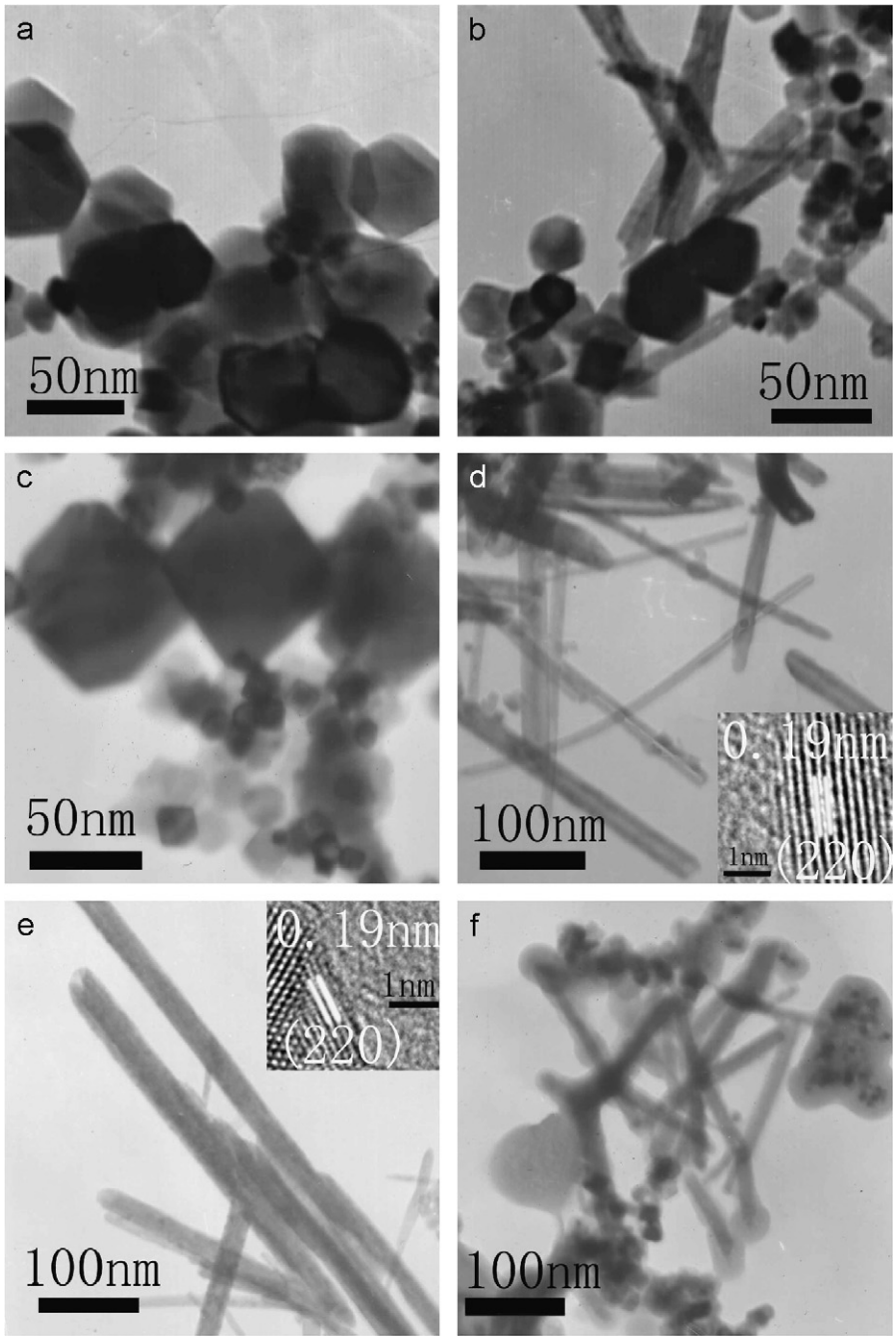

Fig. 6. TEM images of CeO_2 nanoplates under various hydrothermal conditions: (a) nanoplates (100 °C, 72 h, CTAB/Ce^{3+} = 1:3); (b) nanoplates and nanorods (100 °C, 72 h, CTAB/Ce^{3+} = 1:3); (c) irregular nanoplates (100 °C, 2 h, CTAB/Ce^{3+} = 2:3); (d) nanotubes (100 °C, 8 h, CTAB/Ce^{3+} = 2:3, inset is the HRTEM image of nanotubes); (e) nanorods (100 °C, 24 h, CTAB/Ce^{3+} = 2:3, inset is the HRTEM image of nanorods); and (f) nanorods and nanoparticles (100 °C, 72 h, CTAB/Ce^{3+} = 2:3).

energy for the three planes is $\gamma\{111\}<\gamma\{100\}<\gamma\{110\}$ [26,27]. The stable (111) surface limits the size of the large-sized CeO_2 particles, which result in the particle size distribution as shown in Fig. 4.

The capping ability of the CTA^+ is low in our first experimental conditions (S1–S6), so nanoplates become thicker and then partially converted into nanorods. The similar conversion may be due to the anisotropic growth mechanism and driven by the surface energy, which has been reported by some previous studies. Tian et al. [28] obtained large-scale aligned ZnO nanorods fabricated by nanoplates. Gedanken et al. [29] reported the Fe_2O_3 nanoparticles can be converted into uniform-sized nanorods by octylamine mediated process. In our work, the size of the initial nanoplates (Fig. 6a) is 20–50 nm which is equal to the diameter of the final nanorods. This further indicates the nanorods are formed by nanoplates in order to lower the surface energy.

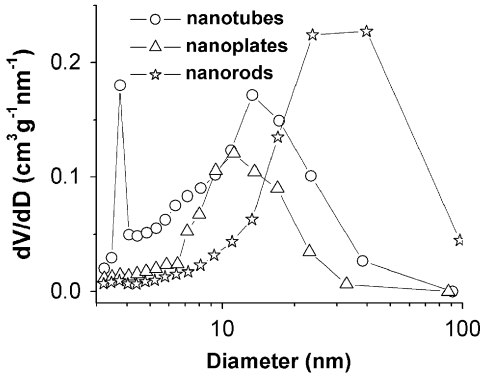

Fig. 7. Plot of the pore volume vs. pore diameter for various CeO_2 nanostructures: nanoplates (S2), nanotubes (S9), and nanorods (S8).

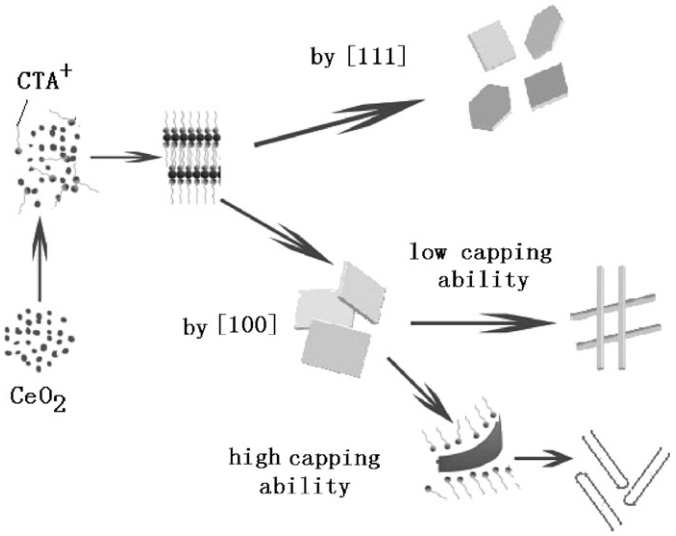

Scheme 1. Possible formation mechanism for CeO_2 nanostructures.

When the capping ability of the CTA^+ increases significantly with the increase of its amount, the nanoplate growth is remarkably restricted, leading to the rolling of it. The TEM images show clearly nanoplates are converted into nanotubes when the time gets longer. The conversion is due to the rolling mechanism and popular for the formation of nanotubes [30], such as MnO_2 nanotubes [31], lanthanide oxides nanotubes [32], and ZnS nanotubes [33]. As the reaction advances, nanotubes grow into nanorods, which may be due to the coarsening of the nanoparticles. Coarsening, also known as Ostwald ripening, is a mechanism driven by the fact that the surface chemical potential of a particle increases with particle size decreasing, which is described by the Gibbs–Thompson equation [34]. To nanotubes, the surface energy of the outer surface is higher than the inner surface. Thus, nanorods are formed by dissolving the outer part of nanotubes and the depositing on the inner part of the nanotubes. Nevertheless when the time is long enough, the nanorods collapse. This is because the nanoparticles tend to combine with (111) not (100) surfaces due to their native characteristics as discussed in the previous paragraph.

As a result, the influence of the reaction time, temperature, and CTAB/Ce^{3+} value on the growth of the CeO_2 crystals may lie in two aspects: influencing the interactions between the nanoplates and affecting the adsorption of CTA^+ onto different crystal facets.

3.3. CO oxidation properties of CeO_2 nanoplates, nanorods, and nanotubes

CO catalytic oxidation is one of the most important properties of CeO_2, which is useful for the TWCs and the fuel battery [2,7]. Fig. 8 and Table 1 show the catalytic activity of CeO_2 nanotubes, nanorods, and nanoplates. In this research, the activities of CeO_2 catalysts are evaluated by the temperature (T_{50}) where 50% CO is converted to CO_2. The T_{50} of nanorods is 273 °C and that of nanotubes is 264 °C, which is nearly 50 °C higher than that of nanoplates (215 °C). It is noted that the T_{50} of CeO_2 nanoparticles in the previous references is always around 300 °C [7,8,23], nearly 100 °C higher than that of CeO_2 nanoplates in our case. It is clear that nanoplates are more active than nanorods and nanotubes.

The above-mentioned XRD analysis shows that the crystal phase of the three products is the same, i.e. a cubic fluorite structure. Thus, it is reasonable to believe that the different catalytic properties of various products may arise from their morphologies and sizes. The CO oxidation activity of CeO_2 is strongly influenced by the crystal plane due to their different ability of creating oxygen vacancies which are the key point for the CO oxidation, as reported by Zhou et al. [23]. Previous computer modeling shows that less energy is required to form oxygen vacancies on (100) than that on (110) and (111) [35,36]. Thus, the nanoplates with the (100) surface exposed are more active than nanotubes and nanorods with (110) surface exposed. The second highest catalytic activity of CeO_2 nanotubes could

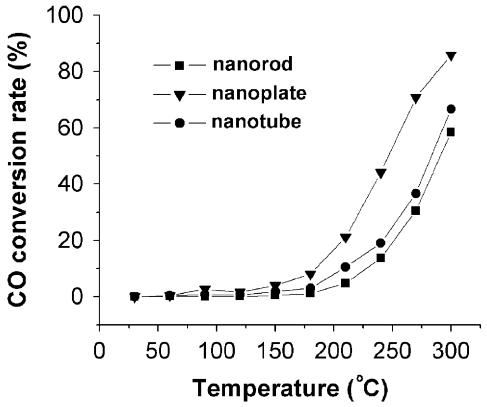

Fig. 8. Plots of CO conversion of various CeO_2 nanostructures vs. temperature: (a) nanoplates (S2), (b) nanotubes (S9), and (c) nanorods (S8).

Table 2
Isoconversion temperatures (°C) extracted from the reaction profiles (Fig. 8) at 10%, 50%, and 90% CO conversion and apparent activation energy values (kJ/mol)

Sample	T_{10}	T_{50}	T_{90}	E_a
Nanoplates (S2)	182	215	302	82.9
Nanorods (S9)	225	273	342	126
Nanotubes (S8)	213	264	326	96

be explained by the reason that the large surface-to-volume area can give more active sites for CO oxidation.

The catalytic reaction process can be written as follows:

$$CeO_2 + \frac{x}{2}CO \rightarrow Ce^{4+}_{1-x}Ce^{3+}_{x}O_{2-(x/2)} + \frac{x}{2}CO_2 + \frac{x}{2}V_o, \quad (1)$$

where x is the fraction reacted and V_o is the oxygen vacancy. For the reaction in this work, Jander's model on solid–gas reaction can be adapted [37]. Ozawa has used this model on the CO oxidation of CeO_2 nanoparticles to calculate the reaction constant, which is represented as [38]

$$[1-(1-x)^{1/3}]^2 = kt, \quad (2)$$

where x is the fraction reacted, k the rate constant, and t is the time. The conversion rate and active energy of CeO_2 nanostructures are shown in Table 2. The active energy of nanoplates decreases obviously as compared to that of nanorods and nanotubes, which proves the crystal surface (100) is easy to create oxygen vacancies and thus favors the catalytic performance. Therefore, the favorable crystal surface together with the large BET specific area is good for the catalytic reaction. When the BET specific area is in the same class, the crystal surface is prior to the catalytic activity of CeO_2.

4. Conclusion

In summary, CeO_2 nanoplates, nanorods, and nanotubes have been synthesized under a hydrothermal condition. Further experiment shows that the conversion of various nanostructures among the as-prepared samples has been realized simply by changing the reaction time, temperature, and CTAB/Ce^{3+} value. The external conditions mainly influence the interactions between nanoplates, and affect the adsorption of CTA^+ onto different crystal facets. An enhanced catalytic activity for CO oxidation has been found for CeO_2 nanoplates compared with CeO_2 nanotubes and nanorods. The crystal plane (100) of CeO_2 may play an important role in determining its catalytic oxidation property. We believe that these structural characteristics of CeO_2 are likely to affect their performance in catalysis and can be extended to other technological applications.

Acknowledgments

The authors acknowledge the supports of Innovative Team Project of Science and Technology Commission of Shanghai, China (No. 06DZ05902) and Shanghai Special Foundation for Selected Cultivation of Excellent Young University Teacher. The authors would like to thank Dr. Q. Li for help with the TEM measurements.

Appendix A. Supplementary materials

The online version of this article contains additional supplementary data. Please visit doi:10.1016/j.jssc.2008.02.011

References

[1] B. Murugan, A.V. Ramaswamy, J. Am. Chem. Soc. 129 (2007) 3062–3063.
[2] H. Yahiro, Y. Baba, K. Eguchi, H. Arai, J. Electrochem. Soc. 135 (1988) 2077–2080.
[3] H. Gu, M.D. Soucek, Chem. Mater. 19 (2007) 1103–1110.
[4] X.D. Feng, D.C. Sayle, Z.L. Wang, M.S. Paras, B. Santora, A.C. Sutorik, T.X.T. Sayle, Y. Yang, Y. Ding, X.D. Wang, Y.S. Her, Science 312 (2006) 1504–1508.
[5] N. Izu, W. Shin, N. Murayama, S. Kanzaki, Sens. Actuator B 87 (2002) 95–98.
[6] S. Tsunekawa, T. Fukuda, A. Kasuya, J. Appl. Phys. 87 (2000) 1318–1321.
[7] A. Trovarelli, Catal. Rev. Sci. Eng. 38 (1996) 439–520.
[8] M.L. Granados, F.C. Galisteo, P.S. Lambrou, R. Mariscal, J. Sanzc, I. Sobrados, J.L.G. Fierro, A.M. Efstathiou, J. Catal. 239 (2006) 410–421.
[9] S. Carrettin, P. Concepción, A. Corma, J.M.L. Nieto, V.F. Puntes, Angew. Chem. Int. Ed. 43 (2004) 2538–2540.
[10] D. Zhang, H. Fu, L. Shi, C. Pan, Q. Li, Y. Chu, W. Yu, Inorg. Chem. 46 (2007) 2446–2451.
[11] W.Q. Han, L. Wu, Y. Zhu, J. Am. Chem. Soc. 127 (2005) 12814–12815.
[12] D. Zhang, L. Shi, H. Fu, J. Fang, Carbon 44 (2006) 2853–2855.
[13] Y.W. Zhang, X. Sun, R. Si, L.P. You, C.H. Yan, J. Am. Chem. Soc. 127 (2005) 3260–3261.
[14] Z.R. Tian, J.A. Voigt, J. Liu, B. Mckenzie, M.J. Mcdermott, J. Am. Chem. Soc. 124 (2002) 12954–12955.
[15] S.W. Yang, L. Gao, J. Am. Chem. Soc. 128 (2006) 9930–9931.
[16] H.X. Mai, L.D. Sun, Y.W. Zhang, R. Si, W. Feng, H.P. Zhang, H.C. Liu, C.H. Yan, J. Phys. Chem. B 109 (2005) 24380–24385.
[17] K. Zhou, Z. Yang, S. Yang, Chem. Mater. 19 (2007) 1215–1217.
[18] D. Zhang, H. Fu, L. Shi, J. Fang, Q. Li, J. Solid State Chem. 180 (2007) 654–660.
[19] H. Fu, D. Zhang, L. Shi, J. Fang, Chem. J. Chinese U. 28 (2007) 617–620.
[20] S. Maensiri, C. Masingboon, P. Laokul, W. Jareonboon, V. Promarak, P.L. Anderson, S. Seraphin, Cryst. Growth Des. 7 (2007) 950–955.
[21] S. Lowell, J.E. Sields, Powder Surface Area and Porosity, Chapman & Hall Ltd., New York, 1991.
[22] M.R. Othman, N.N.N. Mustafa, A.L. Ahmad, Micro. Meso. Mater. 91 (2006) 268–275.
[23] K. Zhou, X. Wang, X. Sun, Q. Peng, Y. Li, J. Catal. 229 (2005) 206–212.
[24] A. Bumajdad, M.I. Zaki, J. Eastoe, L. Pasupulety, Langmuir 10 (2004) 11223–11233.

[25] A. Vantomme, Z.Y. Yuan, G. Du, B.L. Su, Langmuir 21 (2005) 1132–1135.
[26] Z.L. Wang, J. Phys. Chem. B 104 (2000) 1153–1175.
[27] Z.L. Wang, X.D. Feng, J. Phys. Chem. B 107 (2003) 13563–13566.
[28] Z.R. Tian, J.A. Voigt, J. Liu, Nat. Mater. 2 (2003) 821–826.
[29] Z. Zhong, M. Lin, N. Vivien, X.B. Gary, F. Yonglim, A. Gedanken, Chem. Mater. 18 (2006) 6031–6036.
[30] C. Tang, Y. Bando, B. Liu, D. Golberg, Adv. Mater. 17 (2005) 3005–3009.
[31] J.W. Wang, Y.D. Li, Adv. Mater. 15 (2003) 445–447.
[32] X. Wang, Y.D. Li, Chem. Eur. J. 9 (2003) 5627–5635.
[33] X. Wang, Y.D. Li, Inorg. Chem. 45 (2006) 7522–7534.
[34] D.J. Burleson, R.L. Penn, Langmuir 22 (2006) 402–409.
[35] T.X.T. Sayle, S.C. Parker, C.R.A. Catlow, Surf. Sci. 316 (1994) 329–336.
[36] D.C. Sayle, S.A. Maicaneanu, G.W. Watson, J. Am. Chem. Soc. 124 (2002) 11429–11439.
[37] W. Jander, Z. Anorg, Allg. Chem. 163 (1927) 1–30.
[38] M. Ozawa, M. Kimura, A. Isogai, J. Mater. Sci. 26 (1991) 4818–4822.